www.sciencemag.org/content/356/6339/727/suppl/DC1

Supplementary Materials for

Global drainage patterns and the origins of topographic relief on Earth, Mars, and Titan

Benjamin A. Black,* J. Taylor Perron, Douglas Hemingway, Elizabeth Bailey, Francis Nimmo, Howard Zebker

*Corresponding author. Email: bblack@ccny.cuny.edu

Published 19 May 2017, *Science* **356**, 727 (2017)
DOI: 10.1126/science.aag0171

This PDF file includes:

Other Supplementary Materials for this manuscript includes the following:
(available at www.sciencemag.org/content/356/6339/727/suppl/DC1)

Database S1 (Excel)
Database S2 (Zipped archive)

Materials and Methods

Our work relies on three principal datasets: maps of fluvial features on Titan, Earth, and Mars; spherical harmonic models for the topography of each of these bodies; and results from a numerical model of landscape evolution under a range of uplift conditions. We outline our methods for each dataset below.

Mapping fluvial features

Earth. To identify major fluvial features on Earth, we used $1/8^{th}$ degree grids of global flow accumulation, basins, and flow length derived from orbital altimetry and corrected manually *(17)*. We identified each sink as a point of maximum flow accumulation within each basin, and the main trunk as the flow path linking each sink to the most distant point (along flow paths) within each basin. For rivers that spanned more than ~50 km, we identified sampling points at an interval of ~50 km, or every 5^{th} grid point (the results are relatively insensitive to this selection; we chose this interval because it was sufficiently large to avoid sensitivity to the $1/8^{th}$ degree resolution of the drainage dataset). We analyzed only rivers longer than this 50 km interval.

Mars. We relied on a global database of Martian river networks *(18)*. Sinks were identified as the topographically lowest extremities within each network; the validity of these sinks was spot-checked visually. The main trunk of each network was taken to be the path linking the most distal point within a network to the sink. We identified sampling points along this main trunk at an interval that matches the interval we used on Earth, but scaled by the ratio $Radius_{Mars}/Radius_{Earth}$ (this interval equates to ≈30 km on Mars). We analyzed only networks longer than this interval.

Titan. We manually selected 71 drainage networks from a global database compiled from the Cassini spacecraft's Synthetic Aperture Radar (SAR) swaths Ta to T71 *(12)*. These drainages were delineated on the basis of: i) linear geometry cross-cutting other SAR features; ii) light-dark pairings indicative of narrow topographic features; iii) branching geometries; iv) drainage into features interpreted as lakes *(11, 12)*. We selected drainages where we could confidently identify a sink location on the basis of junction angles, progressive downstream widening of valley features, orientation relative to features interpreted as lakes, and/or locally available stereo topography *(34)*. The source and sink coordinates we identified for all 71 networks we analyzed on Titan are given in Database S1. The main trunk of each network was taken to be the path linking the most distant point within a network to the sink. We identified sampling points along this main trunk at an interval that matches the interval we used on Earth, but scaled by the ratio $Radius_{Titan}/Radius_{Earth}$ (this interval equates to ≈21 km on Titan). We analyzed only networks longer than this interval. We defined a subset of North Polar networks as all eligible drainages with sinks located north of 60 °N latitude.

Spherical harmonic topography

We constructed spherical harmonic models of topography for Titan from RADAR-based topography *(21, 31, 35)* referenced to the geoid *(36)*; for Earth from the Earth2012 topography/bathymetry model (referenced to sea level) *(22)*; and for Mars from the Mars Orbiter

Laser Altimeter (MOLA)-derived, aeroid-referenced topography model *(37, 38)*. A robust spherical harmonic expansion for Titan's topography is available only up to degree (ℓ) 6 (ref. *(21)*). Titan has less long-wavelength relief than Earth or Mars (Fig. 1), indicating that the magnitude of topography alone cannot explain conformity. Our spherical harmonic models of terrestrial topography include bathymetry (Fig. S6). Oceanic basins form an integral part of Earth's plate tectonically derived topography (though the weight of the oceans deepens ocean basins, and fluvial erosion does not operate on the seafloor). Ancient oceans may also once have existed on Mars *(3)*.

Data availability

Coordinates for all drainage networks analyzed on Titan are available in spreadsheet form in Database S1. The data required to generate spherical harmonic topography for Earth, Titan, and Mars are available from the references provided in the text.

Landscape evolution model

Our landscape evolution model considers the effects of fluvial incision, uplift, and hill slope erosion (parameterized with a critical slope) on surface topography *(11, 28, 39)*. The model is available at https://github.com/MITGeomorph/Tadpole.

Variable vs. uniform uplift. The landscape evolution model solves the stream-power equation for the time evolution of fluvially eroded topography*(28, 39)*:

$$\frac{dz}{dt} = U - KA^m|\nabla z|^n \qquad \text{(S1)}$$

with elevation z, contributing area A, stream-power coefficient K, rate of uplift relative to a boundary U, m a constant taken to be 0.5*(40)*, and n a constant taken to be 1 *(41)*. Hill slope processes, which occur at finer scales than are of interest for comparison with our global topographic models, are approximated with a critical slope of 0.6, which prevents slopes from becoming unrealistically steep at drainage divides *(11)*.

The power-law relationship between incision rate and channel slope and contributing drainage area in Eq. (1) can be derived from the assumption that channel erosion rates scale with bed shear stress due to flow in a channel *(28, 40)*, and is motivated by the observed negative correlation between channel slope and contributing drainage area on Earth *(42)*. In our simulations, we assume a spatially constant stream-power coefficient, though in practice climatic and lithologic variations can lead to spatial variability in K *(41)*. Plate tectonics produces a patchwork of continental lithologies, and the orogenic feedback loop links mountain-building, exhumation, and climate *(43)*. The first effect might be expected to prolong the effects of plate tectonics in suppressing topographic conformity even after active deformation has ceased; the second effect might be expected to complicate the relationship between rock uplift, topography, and drainage patterns.

We derive a non-dimensional form of the governing equation following *(28)*:

$$\frac{dz'}{dt'} = \frac{KL^{2m}}{U} A'^{m} |\nabla' z'| + 1 \quad \text{(S2)}$$

with $z = z'L$, $A = A'L^2$, $t = t'L/U$, $\nabla = \nabla'/L$. The lengthscale L is chosen to represent the distance from the drainage divide to the sink.

We initialize our simulations with randomly generated, autocorrelated initial topography; the lowest 70% of the initial surface is set to be a topographic sink as an analog for Earth's oceans (Fig. S7). We tabulate model parameter values in Table S1. In the simulations we analyzed, 13 ± 12% (1σ) of the land area is internally drained. For comparison, 14 ± 10% (1σ; the uncertainty reflects variability across continents) of Earth's unglaciated land area is internally drained *(44)*. To approximate the effects of plate tectonics, which localizes crustal thickening, the variable uplift cases have a pseudo-random pattern of autocorrelated, spatially non-uniform uplift superposed on the background uniform uplift field.

In place of spherical harmonic decompositions to characterize the model topography, we used 2-D Fourier transforms as described below.

Impact cratering. Impact cratering is one of the key mechanisms for relief generation on Mars. Crater counting of fluvial landscapes suggests that river activity reached a climax around the Noachian-Hesperian boundary, followed by a decline in activity that roughly coincided with waning cratering activity after the Late Heavy Bombardment *(10, 15)*. Landscape evolution modeling and crater counting further suggests that the terminal period of relatively intense fluvial activity lasted at least 10^3-10^4 years, and more likely spanned 10^5-10^7 years of episodic activity *(45, 46)*. Ancient large-scale topography on Mars, including the hemispheric dichotomy, predates fluvial incision *(1, 5)*. This topography may have been generated through basin-scale impacts *(4)* or through other unknown processes. Geomorphic mapping suggests that valley networks were strongly influenced by ancient topographic gradients, but that younger Noachian-Hesperian cratering did modify and disrupt some river paths *(2, 23)*.

To investigate and quantify the influence of impact cratering on topographic conformity, we ran three landscape evolution model ensembles, each with ten simulations (Fig. S8), in which we considered (i) an initial surface with randomly generated, autocorrelated initial topography (our control ensemble, which represents ancient topography without any younger, fresh craters), (ii) an initial surface with randomly generated, autocorrelated topography, with superposed impact craters (to represent erosion of ancient topography that has experienced more recent cratering), (iii) an initial surface with randomly generated, autocorrelated topography, with superposed impact craters, and with additional impact cratering occurring in tandem with fluvial erosion (to represent cratered, ancient topography that undergoes fluvial erosion in tandem with cratering, for example during the Late Heavy Bombardment).

To account for the greater occurrence of smaller craters, we assumed the size-frequency distribution for Martian impact craters as adapted from the lunar production function for craters 1-16 km in diameter *(47)*. The autocorrelated initial topography represents ancient topography, for example due to basin-forming impacts. However, we did not generate fresh craters larger than 16 km diameter, because our goal was to study the interaction of impacts with pre-existing topography and valley networks (and larger impacts obliterate both for our chosen grid size of 50 km by 50 km). We used scaling relationships for Mars highland craters *(48)* to calculate crater depths for the strength and gravity regimes, and we employed polynomial fits from *(48)* to calculate the shapes of axisymmetric cavities, rims, and uplift zones. Following *(49)*, we

calculated the final topography outside the crater rim as a weighted average of the pre-impact topography and the impact-generated topography, where the weighting declines linearly from the rim to a distance of three radii from the crater center.

Our simulations to investigate impact cratering differ from those designed to investigate the effects of plate tectonic-style deformation in that for the purposes of accurate impact crater depth-diameter scaling, we have chosen to make these simulations dimensional. We used model grids that represented lateral dimensions of 50 km by 50 km, with 125 meter horizontal resolution. Crater interiors in the model are assumed to be flooded and therefore do not erode. The complete list of parameters and parameter values used in the impact cratering simulations is given in Table S2. The true duration and rate of valley network incision on Mars are unknown *(10, 50)*, and the rate and duration trade off in the model to determine the total amount of incision. Trunk channels of Martian valley networks incised ~50 to 350 m into older terrains *(10)*, creating drainage densities of ~10^{-2} km^{-1} *(51)*. We selected values for K (see Table S2) and simulation duration (60 My) that generated cumulative erosion that qualitatively matched typical values of drainage density and trunk channel fluvial incision observed on Mars.

Analysis

The metrics we applied to compare drainage orientations with topography are illustrated graphically in Fig. S1. To avoid the need to weight fluvial features by size, and to integrate changes in flow direction and downslope direction along river courses, we performed both the %d and Λ analyses at intervals along the main trunks of major fluvial features (see Fig. S1).

Synthetic networks. The maximum size of observed drainage networks differs on Titan, Earth, and Mars, which might a priori influence the scale of topography reflected in drainage orientations. To avoid scale dependence in our comparison, we used a point spacing that is uniform relative to planetary radius on each body. To test whether our algorithm displays any bias related to drainage network scale, and to investigate the likelihood of false positive results, we repeated our analyses on synthetic datasets. These datasets comprised line segments of uniform length distributed and oriented randomly across the simulated landscape (Fig. S2). We generated 1,000-10,000 such synthetic segments for each test, and we analyzed the portion of those synthetic segments that crossed the landmasses in our simulations. In total, we conducted four tests on representative simulations from the ensemble analyzed in the manuscript: with line segments spanning either 1/2 or 1/20 the domain of our numerical simulations, and on landscapes in which our simulations included either uniform or variable uplift. In all cases, our analysis yielded statistically indistinguishable results with a topographic conformity of zero (Fig. S2, panels E-F). In other words, the random synthetic networks showed no preferred orientation relative to the topography, and our algorithm displayed no measureable bias due to systematic differences in drainage size. These tests support the robustness of our results for Titan, Earth, and Mars.

Downhill percentage (*%d*). At each upstream-downstream pair of sampling points along each drainage path, we determined whether the upstream point is at a higher elevation according to the topographic model at a given maximum degree. For each body (and each model run) %d is the percentage of all upstream-downstream pairs that pass (i.e. the upstream point has a higher elevation according to the model topography). At infinite resolution (or as wavenumber $k \rightarrow 200$

for the 400×400 model grids), *%d* should approach 100%, because liquid flows downhill with respect to the geoid.

Topographic conformity (Λ). At each sampling point along each drainage path, we determined δ, the angle between the steepest descent direction and the flow direction. For the planetary bodies, steepest descent was determined using MATLAB's `gradientm` function for the gradient on spheroidal bodies; for the model runs, steepest descent was calculated according to the D-infinity flow routing algorithm*(52)*. We calculated flow direction as the azimuth of the vector linking each sampling point to the next downstream point. We defined the topographic conformity at a given maximum spherical harmonic degree or wavenumber as the median value of cosine(δ) calculated at all sampling points: Λ_ℓ = median(cos(δ)).

Uncertainties. The uncertainties indicated in Figure 1, 2, S2, and S3 represent the 95% confidence interval for the median. The 95% confidence interval for the median is bounded by the *j*th and *k*th observation in a ranked list of *n* observations, where *(53, 54)*:
$j = n \times q - 1.96\sqrt{n \times q(1-q)}$, and $k = n \times q + 1.96\sqrt{n \times q(1-q)}$.
Here q = 0.5, because by definition the median divides the dataset into two quantiles.

The uncertainties in Figure 3 represent two standard errors of the mean *%d* (Figure 3c) and Λ (Figure 3d) values across the ensemble of ten simulations with spatially variable uplift and ten simulations with spatially uniform uplift.

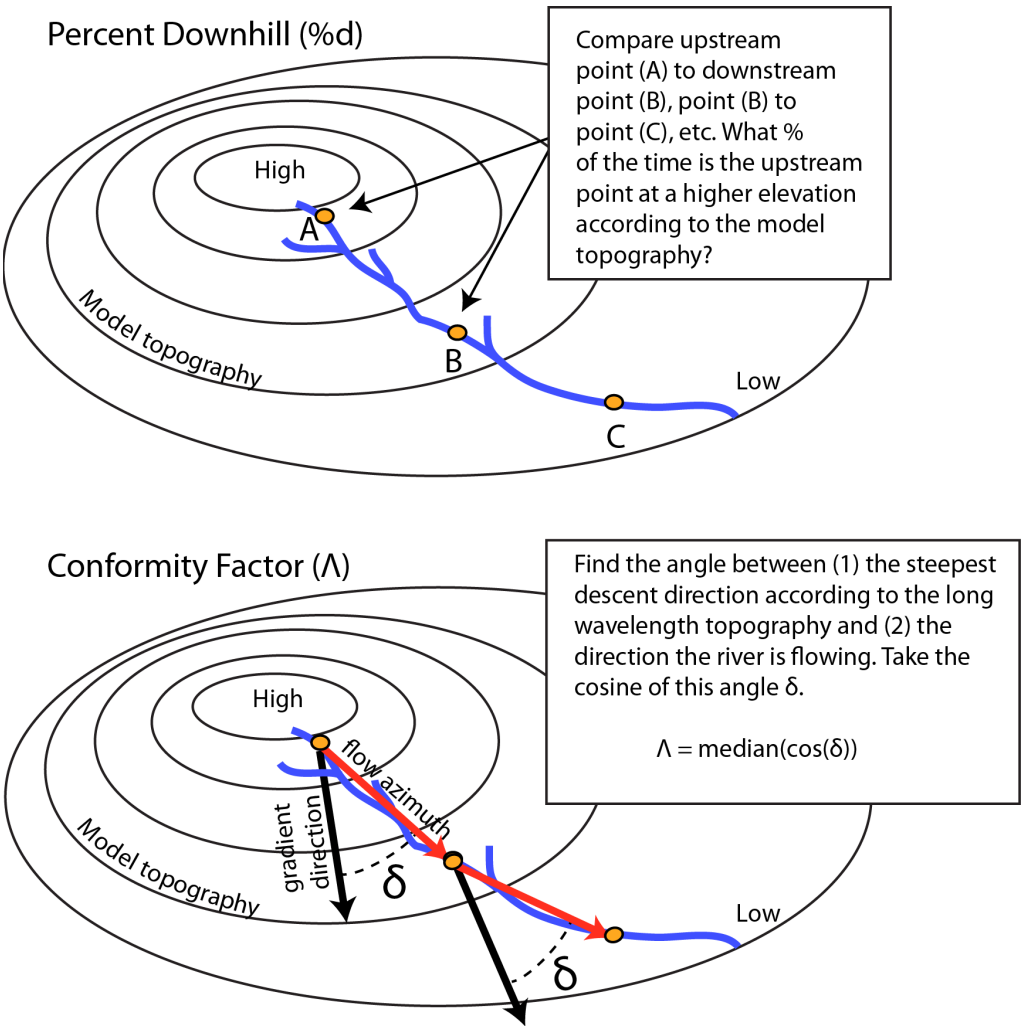

Fig. S1. Schematic illustration of two proxy metrics for the agreement between river orientations and topography at a given scale. The upper panel illustrates the definition of the percent downhill metric (*%d*) and the lower panel the definition of the conformity factor (*Λ*).

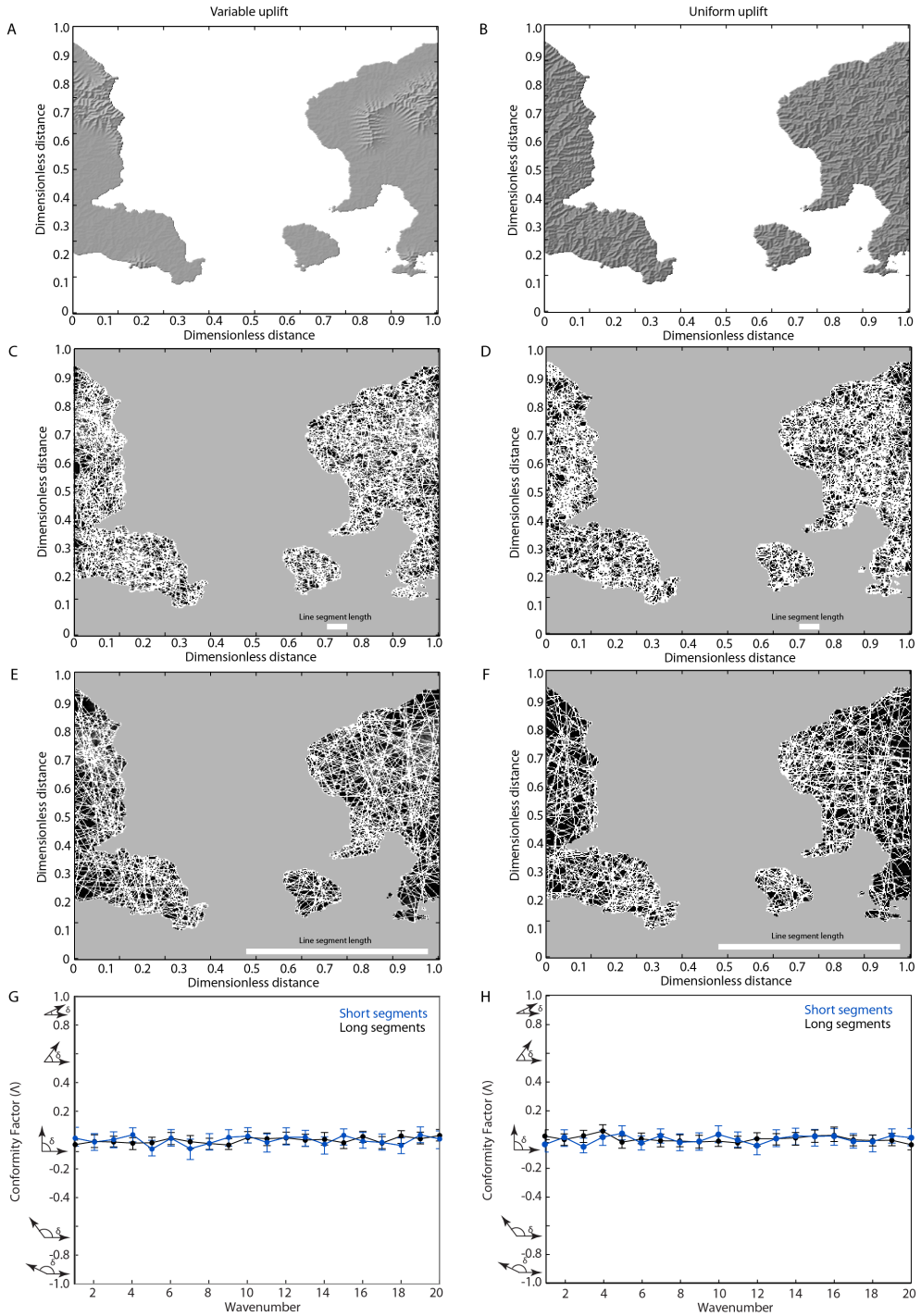

Fig. S2. Synthetic tests to identify any bias related to the scale of measured drainages. (A) Shaded relief map of model topography produced with spatially variable uplift. **(B)** As in A, but for spatially uniform uplift. **(C)** Short synthetic drainages, superposed on outline of topography from A. **(D)** As in C, but with spatially uniform uplift from B. **(E)** As in C, but with long synthetic drainages **(F)** As in E, but for uniform uplift. **(G)** Topographic conformity Λ for synthetic dataset with spatially variable uplift. **(H)** Topographic conformity Λ for synthetic dataset with spatially uniform uplift. Error bars correspond to the 95% confidence interval for the median.

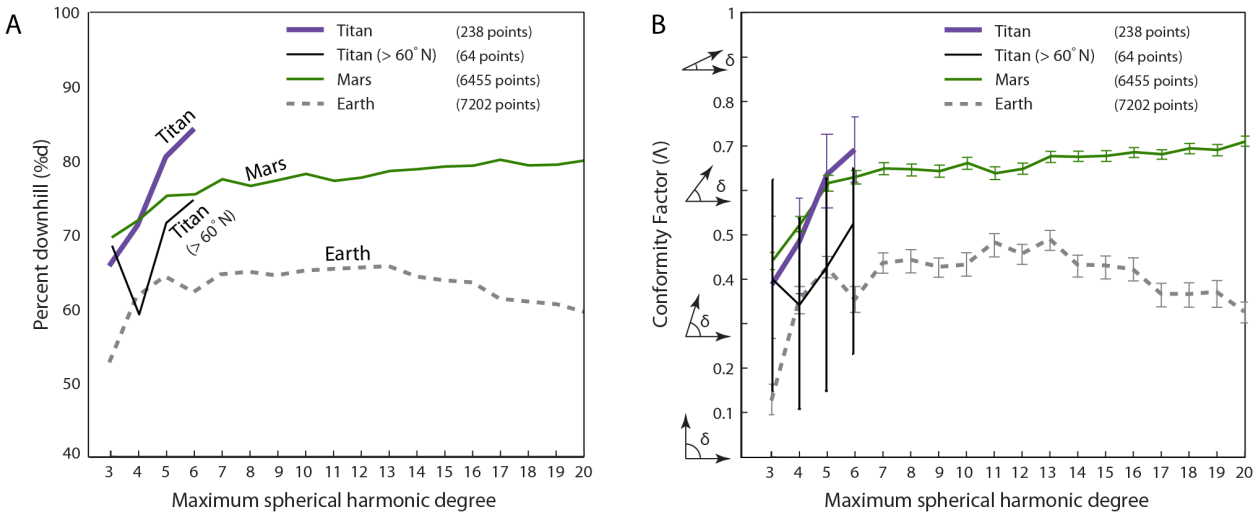

Fig. S3. Long-wavelength topographic conformity is lower in Titan's north polar region. As in Fig. 2, but including Titan's north polar region (defined here as the region northwards of 60°N). Error bars in (B) correspond to the 95% confidence interval for the median. The median conformity factor values for Titan's north polar region at degrees 4-6 are lower than those for Titan as a whole. Given the small sample size, the 95% confidence intervals overlap, but the offset in median values supports differences in the geologic history of Titan's north polar region relative to the rest of Titan.

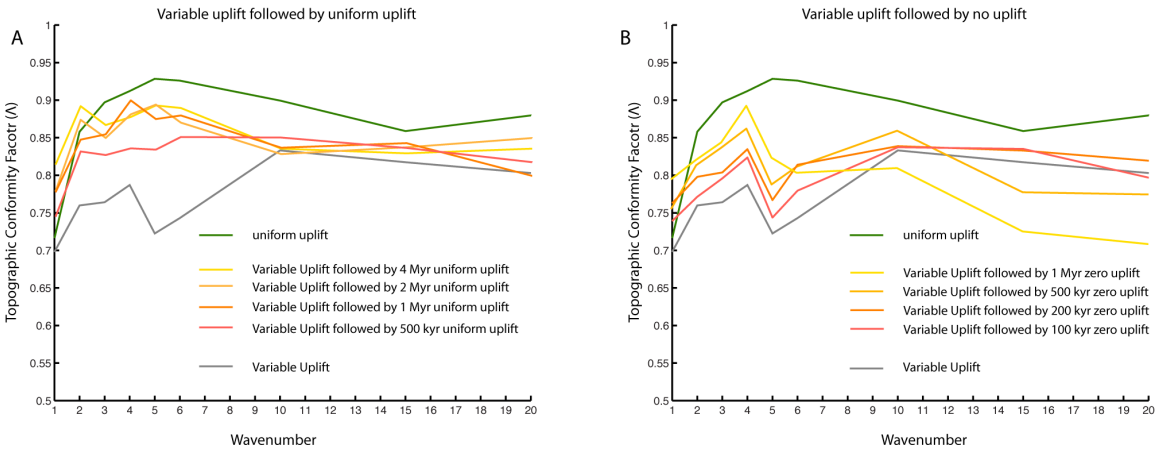

Fig. S4. Drainage networks and deformation interact through time. To investigate how temporal variations in the pattern of deformation influence topographic conformity, we conducted simulations in which variable uplift (which represents dominantly short-wavelength deformation associated with plate tectonics) gave way to either **(A)** uniform uplift, which represents dominantly long-wavelength deformation, or **(B)** zero uplift, which represents tectonic quiescence. Curves represent individual simulations. We find that low Λ is a signature of actively generated variable-uplift plate tectonics. If variable uplift is followed by uniform uplift, then the signature of that variable uplift will gradually be erased. If variable uplift is followed by zero uplift, then Λ increases at first as drainages conform with topography. Ultimately, landscapes where virtually all relief has been erased can also display poor topographic conformity.

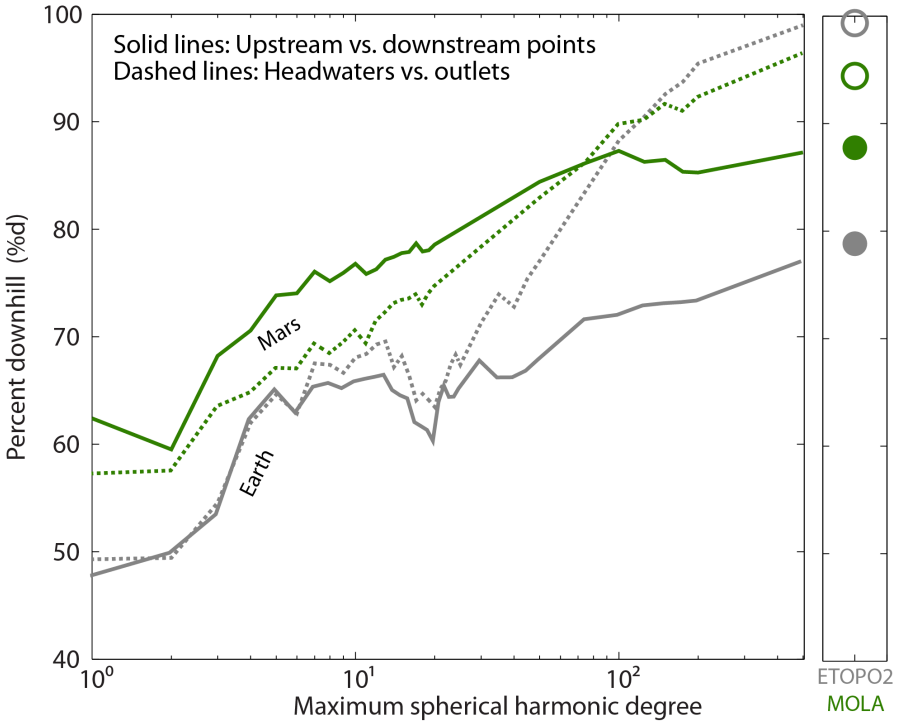

Fig. S5. Differences in topographic conformity on Mars versus Earth extend to shorter wavelengths. Solid lines (and filled circles in right panel) show the percent of points that are uphill (according to the topography at a given spherical harmonic degree) of the nearest downstream point. Dashed lines (and empty circles in right panel) show the percent of headwaters that are uphill (according to the topography at a given spherical harmonic degree) of the drainage network outlet. Small panel at right shows the same metrics computed for the ETOPO2 gridded 2-minute global relief dataset for Earth *(55)* and four pixel-per-degree MOLA topography for Mars *(37)*. We expect *%d* to reach 100% when topography is perfectly resolved, drainage networks are perfectly delineated, and drainages have not experienced deformation after the era of fluvial activity. On Earth, the delineation of fluvial features was performed at 1/8 degree resolution from HydroSHEDS and Hydro1k data *(17)*, distinct from the higher resolution ETOPO2 dataset, resulting in slight misalignments at the scale at which fluvial valleys are resolved. These misalignments do not affect long wavelength topographic conformity, because fluvial valleys are not resolved at these wavelengths. We attribute the plateau in %d on Mars to deformation after incision of valley networks *(24, 25)*. For Earth and Mars, calculation of *%d* for the headwaters versus outlet of each drainage shows that *%d* values on Earth converge to 100% across the scale of the drainage, whereas *%d* values on Mars reach ~95%.

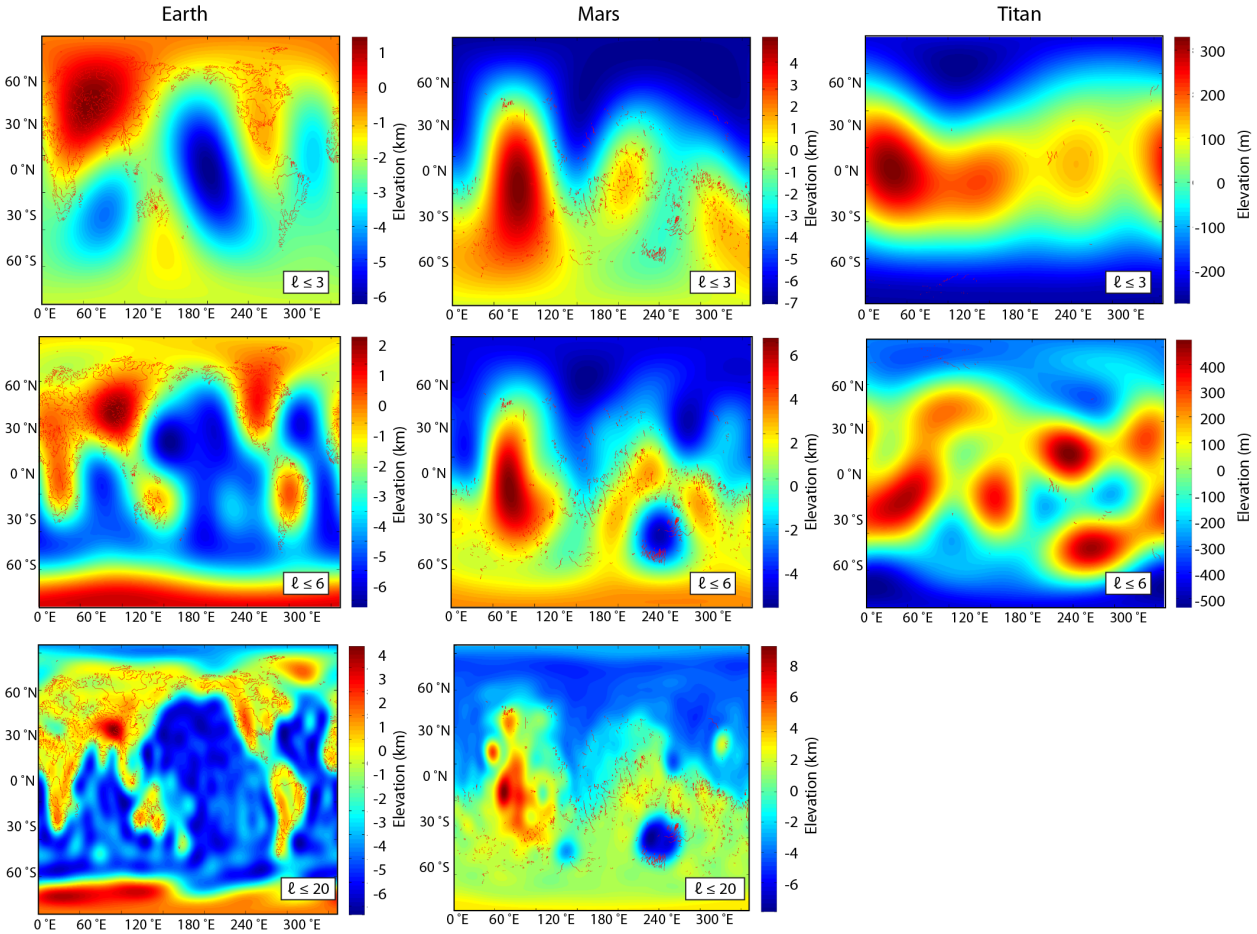

Fig. S6. Spherical harmonic models for the topography of Titan, Earth, and Mars. For Earth and Mars, we show maximum spherical harmonic degrees (ℓ) of 3,6, and 20. At present, topography is not well constrained for ℓ>6 for Titan *(21)*. Coloring reflects elevation referenced to the geoid.

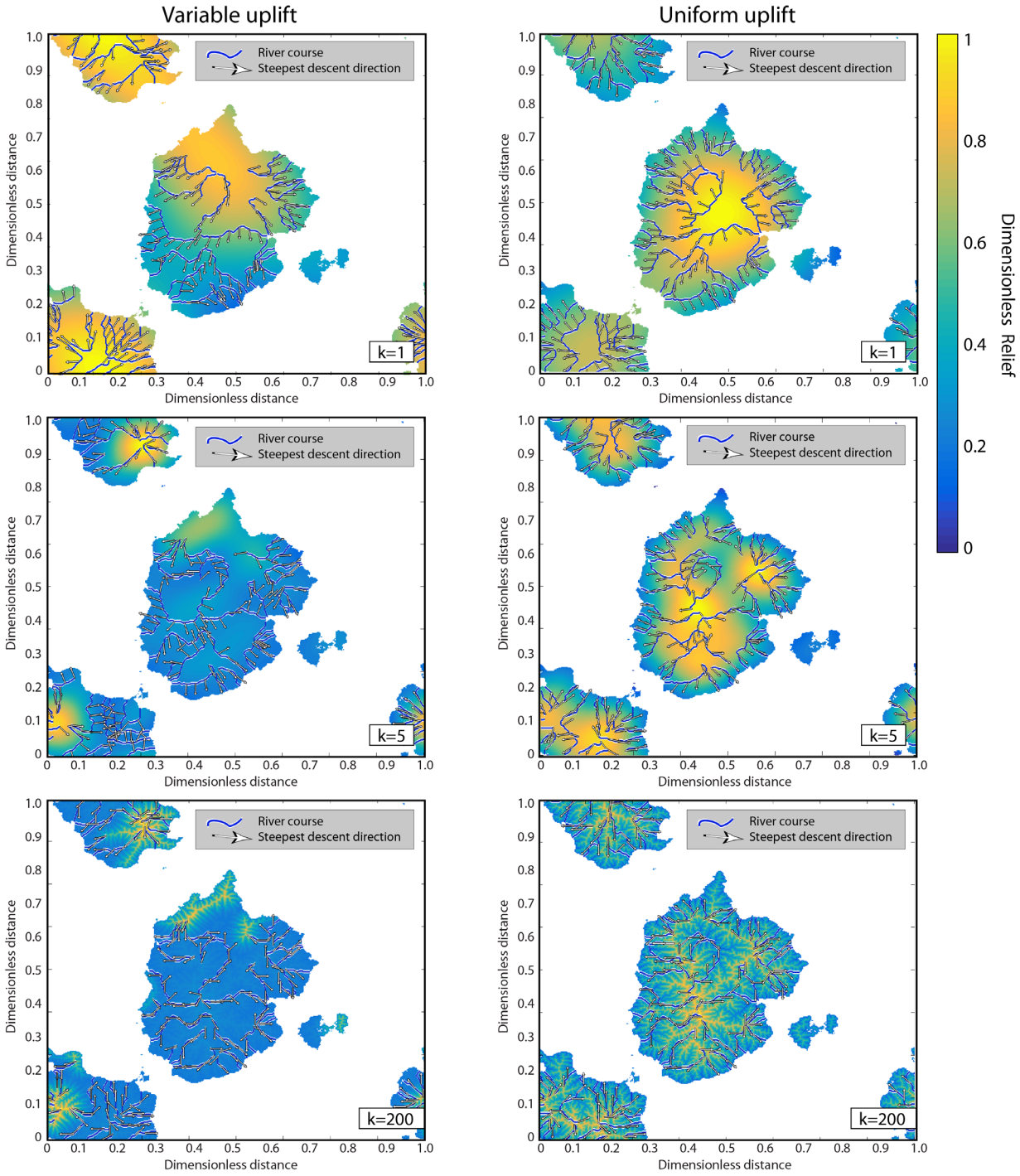

Fig. S7. Example model topography, filtered to increasing maximum spectral wavenumbers. We show the model state at the conclusion of variable uplift (left column) and uniform uplift (right column) runs with identical initial conditions. We filter the topography to maximum spectral wavenumbers of k=1, k=5, and k=200 wavelengths across the domain, as indicated on each panel.

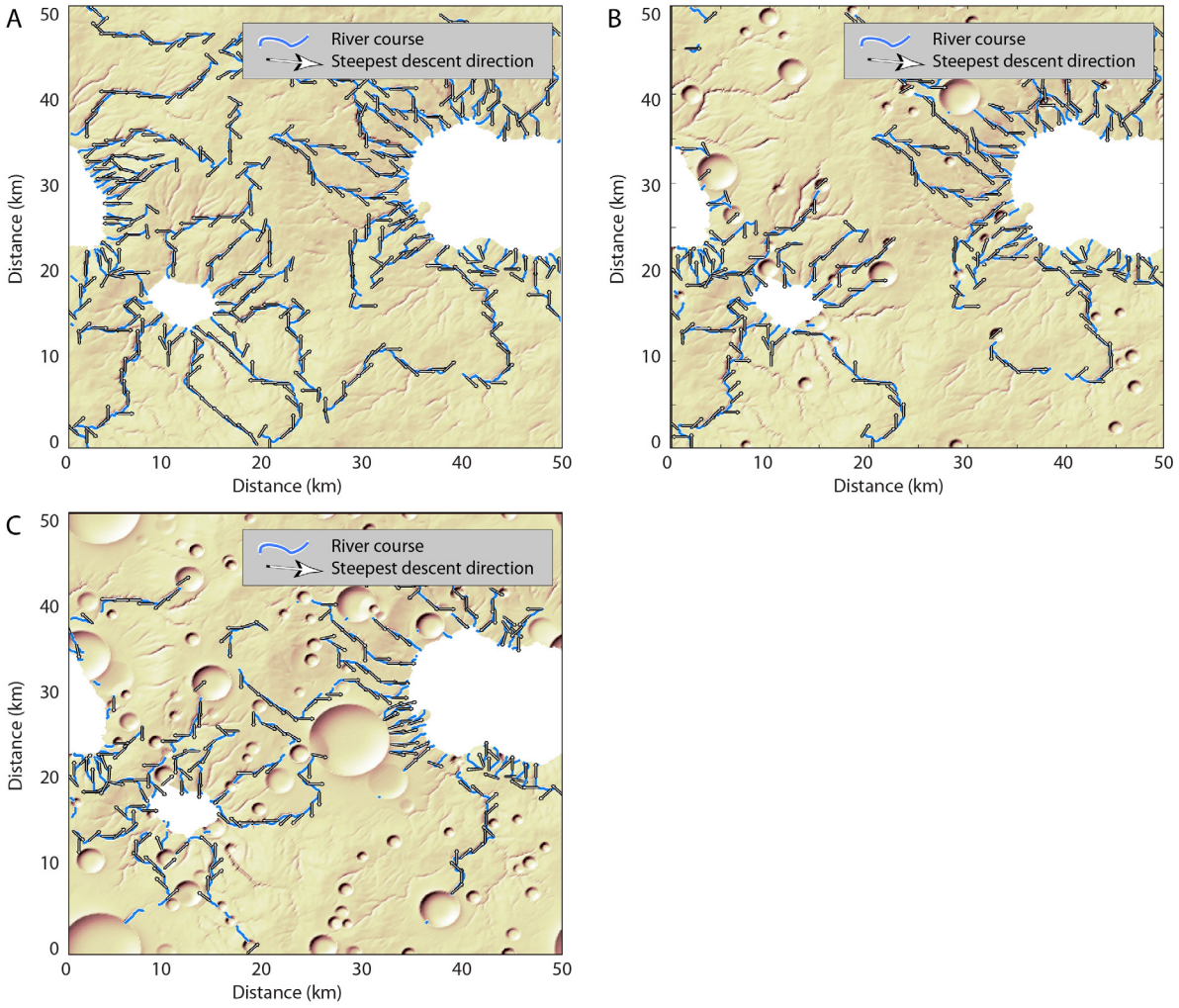

Fig. S8. Shaded relief maps of landscape evolution simulations with cratering. We ran three ensembles (each with ten simulations spanning 60 My) to examine the influence of impact cratering on topographic conformity. **(A)** In the control ensemble, fluvial erosion of an initially uncratered surface proceeded without interference. **(B)** We considered fluvial erosion of the same initial surfaces in the control ensemble, but with impact topography superposed on the initial surface as described in the Materials and Methods. **(C)** We also considered fluvial erosion of the same cratered initial surfaces, but with further impacts that occurred during the course of our simulations, disrupting the topography (note the presence of truncated valley networks). This simulation is also shown in Fig. 4A. Each snapshot shows the state of the simulation after 60 My.

Table S1. Landscape evolution modeling parameters.

Parameter	Value	Notes
Lateral grid dimensions	400 × 400	
Enhanced uplift relative to background uplift	10	Only in variable uplift simulations
Steam power coefficient K	5×10^{-6} $m^{(1-2m)}$ yr^{-1}	
Drainage area exponent m	0.5	ref. *(40)*
Slope exponent n	1.0	ref. *(41)*
Critical slope	0.6	
Slope of the power spectrum of initial red noise topography	2.0	ref. *(27)*
Fraction of initial topography assigned to be a fixed base level (to represent oceans)	0.7	
Slope of the power spectrum of red noise surface used to define zones of enhanced uplift in variable uplift simulations	1.3	Only in variable uplift simulations. Less positive values translate to more variance at shorter wavelengths
Fraction of this surface assigned to experience enhanced uplift in variable uplift simulations	0.35	Only in variable uplift simulations.
Simulation duration	10 My	

Table S2. Landscape evolution modeling parameters for impact cratering simulations.

Parameter	Value	Notes
Lateral grid dimensions	400 × 400	
Lateral grid spacing	125 m × 125 m	
Steam power coefficient K	1×10^{-8} $m^{(1-2m)}$ yr^{-1}	
Drainage area exponent m	0.5	ref. *(40)*
Slope exponent n	1.0	ref. *(41)*
Critical slope	0.6	
Slope of the power spectrum of initial red noise topography	2.0	ref. *(27)*
Fraction of initial topography assigned to be a fixed base level (to represent lakes or oceans)	0.1	
Simulation duration	60 My	

Database S1. Source and sink coordinates for analyzed drainage networks on Titan (see Excel file with tabulated coordinates).

Database S2. Spherical harmonic expansion coefficients representing Titan's topography with respect to its geoid.

References and Notes

1. R. J. Phillips, M. T. Zuber, S. C. Solomon, M. P. Golombek, B. M. Jakosky, W. B. Banerdt, D. E. Smith, R. M. Williams, B. M. Hynek, O. Aharonson, S. A. Hauck II, Ancient geodynamics and global-scale hydrology on Mars. *Science* **291**, 2587–2591 (2001). doi:10.1126/science.1058701 Medline

2. R. P. Irwin, A. D. Howard, Drainage basin evolution in Noachian Terra Cimmeria, Mars. *J. Geophys. Res. Planets* **107**, 10-1–10-23 (2002). doi:10.1029/2001JE001818

3. J. T. Perron, J. X. Mitrovica, M. Manga, I. Matsuyama, M. A. Richards, Evidence for an ancient martian ocean in the topography of deformed shorelines. *Nature* **447**, 840–843 (2007). doi:10.1038/nature05873 Medline

4. J. C. Andrews-Hanna, M. T. Zuber, W. B. Banerdt, The Borealis basin and the origin of the martian crustal dichotomy. *Nature* **453**, 1212–1215 (2008). doi:10.1038/nature07011 Medline

5. S. Bouley, D. Baratoux, I. Matsuyama, F. Forget, A. Séjourné, M. Turbet, F. Costard, Late Tharsis formation and implications for early Mars. *Nature* **531**, 344–347 (2016). doi:10.1038/nature17171 Medline

6. G. C. Collins, W. B. McKinnon, J. M. Moore, F. Nimmo, R. T. Pappalardo, L. M. Prockter, P. M. Schenk, "Tectonics of the outer planet satellites," in *Planetary Tectonics*, T. R. Watters, R. A. Schultz, Eds. (Cambridge Univ. Press, 2009), pp. 264–350.

7. F. Nimmo, B. Bills, Shell thickness variations and the long-wavelength topography of Titan. *Icarus* **208**, 896–904 (2010). doi:10.1016/j.icarus.2010.02.020

8. J. M. Moore, W. B. McKinnon, J. R. Spencer, A. D. Howard, P. M. Schenk, R. A. Beyer, F. Nimmo, K. N. Singer, O. M. Umurhan, O. L. White, S. A. Stern, K. Ennico, C. B. Olkin, H. A. Weaver, L. A. Young, R. P. Binzel, M. W. Buie, B. J. Buratti, A. F. Cheng, D. P. Cruikshank, W. M. Grundy, I. R. Linscott, H. J. Reitsema, D. C. Reuter, M. R. Showalter, V. J. Bray, C. L. Chavez, C. J. A. Howett, T. R. Lauer, C. M. Lisse, A. H. Parker, S. B. Porter, S. J. Robbins, K. Runyon, T. Stryk, H. B. Throop, C. C. C. Tsang, A. J. Verbiscer, A. M. Zangari, A. L. Chaikin, D. E. Wilhelms, New Horizons Science Team, The geology of Pluto and Charon through the eyes of New Horizons. *Science* **351**, 1284–1293 (2016). doi:10.1126/science.aad7055 Medline

9. S. D. Willett, S. W. McCoy, J. T. Perron, L. Goren, C. Y. Chen, Dynamic reorganization of river basins. *Science* **343**, 1248765 (2014). doi:10.1126/science.1248765 Medline

10. A. D. Howard, J. M. Moore, R. P. Irwin, An intense terminal epoch of widespread fluvial activity on early Mars: 1. Valley network incision and associated deposits. *J. Geophys. Res. Planets* **110**, E12S14 (2005). doi:10.1029/2005JE002459

11. B. A. Black, J. T. Perron, D. M. Burr, S. A. Drummond, Estimating erosional exhumation on Titan from drainage network morphology. *J. Geophys. Res. Planets* **117**, E08006 (2012). doi:10.1029/2012JE004085

12. D. M. Burr, S. A. Drummond, R. Cartwright, B. A. Black, J. T. Perron, Morphology of fluvial networks on Titan: Evidence for structural control. *Icarus* **226**, 742–759 (2013). doi:10.1016/j.icarus.2013.06.016

13. C. Hoorn, F. P. Wesselingh, H. ter Steege, M. A. Bermudez, A. Mora, J. Sevink, I. Sanmartín, A. Sanchez-Meseguer, C. L. Anderson, J. P. Figueiredo, C. Jaramillo, D. Riff, F. R. Negri, H. Hooghiemstra, J. Lundberg, T. Stadler, T. Särkinen, A. Antonelli, Amazonia through time: Andean uplift, climate change, landscape evolution, and biodiversity. *Science* **330**, 927–931 (2010). doi:10.1126/science.1194585 Medline

14. H. V. Frey, J. H. Roark, K. M. Shockey, E. L. Frey, S. E. Sakimoto, Ancient lowlands on Mars. *Geophys. Res. Lett.* **29**, 22-1–22-4 (2002). doi:10.1029/2001GL013832

15. C. I. Fassett, J. W. Head III, The timing of martian valley network activity: Constraints from buffered crater counting. *Icarus* **195**, 61–89 (2008). doi:10.1016/j.icarus.2007.12.009

16. C. D. Neish, R. D. Lorenz, Titan's global crater population: A new assessment. *Planet. Space Sci.* **60**, 26–33 (2012). doi:10.1016/j.pss.2011.02.016

17. H. Wu, J. S. Kimball, H. Li, M. Huang, L. R. Leung, R. F. Adler, A new global river network database for macroscale hydrologic modeling. *Water Resour. Res.* **48**, W09701 (2012). doi:10.1029/2012WR012313

18. B. M. Hynek, M. Beach, M. R. Hoke, Updated global map of Martian valley networks and implications for climate and hydrologic processes. *J. Geophys. Res. Planets* **115**, E09008 (2010). doi:10.1029/2009JE003548

19. Materials and methods are available as supplementary materials.

20. M. A. Wieczorek, "Gravity and topography of the terrestrial planets," in *Treatise on Geophysics*, G. Schubert, Ed. (Elsevier, ed. 2, 2015), chap. 10.05, pp. 153–193.

21. H. A. Zebker, B. Stiles, S. Hensley, R. Lorenz, R. L. Kirk, J. Lunine, Size and shape of Saturn's moon Titan. *Science* **324**, 921–923 (2009). doi:10.1126/science.1168905 Medline

22. C. Hirt, M. Kuhn, W. Featherstone, F. Göttl, Topographic/isostatic evaluation of new-generation GOCE gravity field models. J. Geophys. Res. Solid Earth **117**, B05407 (2012). doi:10.1029/2011JB008878

23. R. P. Irwin III, R. A. Craddock, A. D. Howard, H. L. Flemming, Topographic influences on development of Martian valley networks. *J. Geophys. Res. Planets* **116**, E02005 (2011). doi:10.1029/2010JE003620

24. W. Luo, T. Stepinski, Orientation of valley networks on Mars: The role of impact cratering. *Geophys. Res. Lett.* **39**, L24201 (2012). doi:10.1029/2012GL054087

25. A. Lefort, D. M. Burr, F. Nimmo, R. E. Jacobsen, Channel slope reversal near the Martian dichotomy boundary: Testing tectonic hypotheses. *Geomorphology* **240**, 121–136 (2014). doi:10.1016/j.geomorph.2014.09.028

26. G. Tobie, J. I. Lunine, C. Sotin, Episodic outgassing as the origin of atmospheric methane on Titan. *Nature* **440**, 61–64 (2006). doi:10.1038/nature04497 Medline

27. D. L. Turcotte, A fractal interpretation of topography and geoid spectra on the Earth, Moon, Venus, and Mars. *J. Geophys. Res. Solid Earth* **92**, E597–E601 (1987). doi:10.1029/JB092iB04p0E597

28. J. T. Perron, W. E. Dietrich, J. W. Kirchner, Controls on the spacing of first-order valleys. *J. Geophys. Res. Earth Surf.* **113**, F04016 (2008). doi:10.1029/2007JF000977

29. F. Nimmo, D. Stevenson, Influence of early plate tectonics on the thermal evolution and magnetic field of Mars. *J. Geophys. Res. Planets* **105**, 11969–11979 (2000). doi:10.1029/1999JE001216

30. V. Sautter, M. J. Toplis, R. C. Wiens, A. Cousin, C. Fabre, O. Gasnault, S. Maurice, O. Forni, J. Lasue, A. Ollila, J. C. Bridges, N. Mangold, S. Le Mouélic, M. Fisk, P.-Y. Meslin, P. Beck, P. Pinet, L. Le Deit, W. Rapin, E. M. Stolper, H. Newsom, D. Dyar, N. Lanza, D. Vaniman, S. Clegg, J. J. Wray, *In situ* evidence for continental crust on early Mars. *Nat. Geosci.* **8**, 605–609 (2015). doi:10.1038/ngeo2474

31. D. Hemingway, F. Nimmo, H. Zebker, L. Iess, A rigid and weathered ice shell on Titan. *Nature* **500**, 550–552 (2013). doi:10.1038/nature12400 Medline

32. T. Schneider, S. D. B. Graves, E. L. Schaller, M. E. Brown, Polar methane accumulation and rainstorms on Titan from simulations of the methane cycle. *Nature* **481**, 58–61 (2012). doi:10.1038/nature10666 Medline

33. R. D. Lorenz, E. P. Turtle, B. Stiles, A. Le Gall, A. Hayes, O. Aharonson, C. A. Wood, E. Stofan, R. Kirk, Hypsometry of Titan. *Icarus* **211**, 699–706 (2011). doi:10.1016/j.icarus.2010.10.002

34. B. W. Stiles, S. Hensley, Y. Gim, D. M. Bates, R. L. Kirk, A. Hayes, J. Radebaugh, R. D. Lorenz, K. L. Mitchell, P. S. Callahan, H. Zebker, W. T. K. Johnson, S. D. Wall, J. I. Lunine, C. A. Wood, M. Janssen, F. Pelletier, R. D. West, C. Veeramacheneni, Determining Titan surface topography from Cassini SAR data. *Icarus* **202**, 584–598 (2009). doi:10.1016/j.icarus.2009.03.032

35. H.A. Zebker, L. Iess, S. D. Wall, R. D. Lorenz, J. I. Lunine, B. W. Stiles, "Titan's Figure Fatter, Flatter Than Its Gravity Field," American Geophysical Union Fall Meeting, abstract P23F-01 (2012).

36. L. Iess, R. A. Jacobson, M. Ducci, D. J. Stevenson, J. I. Lunine, J. W. Armstrong, S. W. Asmar, P. Racioppa, N. J. Rappaport, P. Tortora, The tides of Titan. *Science* **337**, 457–459 (2012). doi:10.1126/science.1219631 Medline

37. D. E. Smith, M. T. Zuber, S. C. Solomon, R. J. Phillips, J. W. Head, J. B. Garvin, W. B. Banerdt, D. O. Muhleman, G. H. Pettengill, G. A. Neumann, F. G. Lemoine, J. B. Abshire, O. Aharonson, C. D. Brown, S. A. Hauck, A. B. Ivanov, P. J. McGovern, H. J. Zwally, T. C. Duxbury, The global topography of Mars and implications for surface evolution. *Science* **284**, 1495–1503 (1999). doi:10.1126/science.284.5419.1495 Medline

38. D. Smith, G. Neumann, R. Arvidson, E. Guinness, S. Slavney, Mars Global Surveyor laser altimeter mission experiment gridded data record (NASA Planetary Data System, 2003).

39. J. T. Perron, J. W. Kirchner, W. E. Dietrich, Formation of evenly spaced ridges and valleys. *Nature* **460**, 502–505 (2009). doi:10.1038/nature08174

40. A. D. Howard, G. Kerby, Channel changes in badlands. *Geol. Soc. Am. Bull.* **94**, 739–752 (1983). doi:10.1130/0016-7606(1983)94<739:CCIB>2.0.CO;2

41. K. L. Ferrier, K. L. Huppert, J. T. Perron, Climatic control of bedrock river incision. *Nature* **496**, 206–209 (2013). doi:10.1038/nature11982 Medline

42. K. X. Whipple, G. E. Tucker, Dynamics of the stream-power river incision model: Implications for height limits of mountain ranges, landscape response timescales, and research needs. *J. Geophys. Res. Solid Earth* **104**, 17661–17674 (1999). doi:10.1029/1999JB900120

43. S. D. Willett, Orogeny and orography: The effects of erosion on the structure of mountain belts. *J. Geophys. Res. Solid Earth* **104**, 28957–28981 (1999). doi:10.1029/1999JB900248

44. C. Vörösmarty, B. Fekete, M. Meybeck, R. Lammers, Global system of rivers: Its role in organizing continental land mass and defining land-to-ocean linkages. *Global Biogeochem. Cycles* **14**, 599–621 (2000). doi:10.1029/1999GB900092

45. C. J. Barnhart, A. D. Howard, J. M. Moore, Long-term precipitation and late-stage valley network formation: Landform simulations of Parana Basin, Mars. *J. Geophys. Res. Planets* **114**, E01003 (2009). doi:10.1029/2008JE003122

46. E. S. Kite, A. Lucas, C. I. Fassett, Pacing early Mars river activity: Embedded craters in the Aeolis Dorsa region imply river activity spanned ≳(1–20) Myr. *Icarus* **225**, 850–855 (2013). doi:10.1016/j.icarus.2013.03.029

47. B. A. Ivanov, Mars/Moon cratering rate ratio estimates. *Space Sci. Rev.* **96**, 87–104 (2001). doi:10.1023/A:1011941121102

48. S. T. Stewart, G. J. Valiant, Martian subsurface properties and crater formation processes inferred from fresh impact crater geometries. *Meteorit. Planet. Sci.* **41**, 1509–1537 (2006). doi:10.1111/j.1945-5100.2006.tb00433.x

49. N. K. Forsberg-Taylor, A. D. Howard, R. A. Craddock, Crater degradation in the Martian highlands: Morphometric analysis of the Sinus Sabaeus region and simulation modeling suggest fluvial processes. *J. Geophys. Res. Planets* **109**, E05002 (2004). doi:10.1029/2004JE002242

50. N. Mangold, E. S. Kite, M. G. Kleinhans, H. Newsom, V. Ansan, E. Hauber, E. Kraal, C. Quantin, K. Tanaka, The origin and timing of fluvial activity at Eberswalde crater, Mars. *Icarus* **220**, 530–551 (2012). doi:10.1016/j.icarus.2012.05.026

51. B. M. Hynek, R. J. Phillips, New data reveal mature, integrated drainage systems on Mars indicative of past precipitation. *Geology* **31**, 757–760 (2003). doi:10.1130/G19607.1

52. D. G. Tarboton, A new method for the determination of flow directions and upslope areas in grid digital elevation models. *Water Resour. Res.* **33**, 309–319 (1997). doi:10.1029/96WR03137

53. W. J. Conover, *Practical Nonparametric Statistics* (Wiley, ed. 2, 1980).

54. M. Longnecker, R. Ott, *An Introduction to Statistical Methods and Data Analysis* (Nelson Education, Toronto, ed. 5, 2001).

55. W. H. Smith, D. T. Sandwell, Global sea floor topography from satellite altimetry and ship depth soundings. *Science* **277**, 1956–1962 (1997). doi:10.1126/science.277.5334.1956